Journal of Alloys and Compounds 619 (2015) 345–355

Heterogeneous nucleation of Cu_6Sn_5 in Sn-Cu-Al solders

J.W. Xian[1*], S.A. Belyakov[1], T.B. Britton[1] and C.M. Gourlay[1]

[1] Department of Materials, Imperial College, London. SW7 2AZ UK.

Abstract

Cu_6Sn_5 is a common intermetallic in Pb-free soldering. We explore the influence of dilute aluminium additions on the heterogeneous nucleation and grain refinement of primary Cu_6Sn_5 in Sn-4Cu-xAl solders. For cooling rates relevant to soldering, it is found that 0.02 and 0.2wt%Al cause significant grain refinement of Cu_6Sn_5 with 0.2wt%Al increasing the number of Cu_6Sn_5 grains per unit area by a factor of ~8. Grain refinement is shown to be due to heterogeneous nucleation of Cu_6Sn_5 on either delta-$Cu_{33}Al_{17}$ or gamma1-Cu_9Al_4, coupled with significant constitutional supercooling ahead of growing Cu_6Sn_5 crystals. Reproducible orientation relationships are measured between the Cu-Al intermetallics and Cu_6Sn_5, with a planar lattice mismatch of less than 2.5%. The role of potent nuclei and solutal growth restriction are discussed with reference to the grain refinement of structural casting alloys.

Keywords: Intermetallics, crystal growth, microstructure, electron backscatter diffraction (EBSD), Pb-free soldering, solidification

Contact Details

***** Corresponding author

jingwei.xian11@imperial.ac.uk

Tel: +447724714613

1. Introduction

Cu_6Sn_5 is a key intermetallic in Pb-free soldering. It is the main intermetallic phase in the reaction layer between the solder and Cu substrates, and it also forms in the bulk solder, as a primary phase and/or as part of the eutectic mixture in both Sn-Ag-Cu and Sn-Cu solders [1].

Cu_6Sn_5 exists in at least four polymorphs [2]. The phase that forms during solder reactions and subsequent solidification is hexagonal η-Cu_6Sn_5 (Pearson symbol *hP*4, Space group $P6_3/mmc$) [3] and transforms to one or more monoclinic phases at lower temperature [2]. There has been significant interest in controlling phase transformations in Cu_6Sn_5 [2, 4] and, additionally, it would be beneficial to be able to control the size and shape of Cu_6Sn_5 grains in the interfacial layer and bulk solder to tailor the mechanical performance of joints.

There has been recent interest in adding dilute Al additions to Pb-free solders [1, 5-8] due to a range of potentially beneficial effects. For example, it is reported that Al additions of 0.01–2 wt%Al are effective at reducing the nucleation undercooling for βSn in Sn-3.5Ag [5] and Sn-Ag-Cu [1, 6] solders and can suppress Cu_6Sn_5 layer growth on Cu substrates [7, 8].

In Cu-containing solders or during soldering to Cu substrates, Al additions usually cause one or more Cu_xAl_y intermetallics to form. Four Cu-Al intermetallics have been reported in solders, θ-$CuAl_2$, η_2-CuAl, δ-$Cu_{33}Al_{17}$ and γ_1-Cu_9Al_4, depending on the base solder, Al addition and substrate as summarised in Table 1 [5, 6, 8-18]. It can be inferred from Table 1 that, for Sn-Ag-Cu solders solidified without reactive substrates, $CuAl_2$ is observed at Al levels above ~1wt% [12] while CuAl is found at Al levels between 0.1-1wt% [13, 18], and that the situation is more complex during soldering to Cu substrates due to substrate dissolution. Furthermore, the reaction between Al and Cu is reported to reduce the phase fraction of Cu_6Sn_5 formed in the

bulk solder [12, 13] and, in Sn-Ag-Cu solders, Al additionally reacts with Ag to form Ag_3Al [5, 14].

It has recently been reported that Cu_xAl_y intermetallics can significantly influence the Cu_6Sn_5 phase in solders [6, 17]. Boesenberg et al. [17] observed that δ-$Cu_{33}Al_{17}$ often shared an interface with Cu_6Sn_5 in Sn-3.5Ag-0.95Cu, Kantarcıoğlu and Kalay [6] reported that 0.05 wt% Al additions to Sn-3.5Ag-0.9Cu/Cu joints decreases the primary Cu_6Sn_5 size and McDonald et al. [10] found that Al additions could refine the Cu_6Sn_5 grain size in hypereutectic Sn-Cu alloys. However, despite the many studies summarised in Table 1, there is little fundamental understanding of how Al additions influence the nucleation and growth of Cu_6Sn_5. In this paper we explore these initial findings in detail with the following specific aims: (i) to quantify the effectiveness of Al additions at decreasing the Cu_6Sn_5 grain size, (ii) to deduce the mechanisms responsible for enhanced heterogeneous nucleation of Cu_6Sn_5 and (iii) to compare these mechanisms with the widely studied grain refinement of structural casting alloys.

2. Methods

The influence of Al additions on the nucleation and grain refinement of primary Cu_6Sn_5 was studied in Sn-4Cu solders containing 0-0.2wt%Al. Since past work [10] has shown that Al additions decrease the Cu_6Sn_5 liquids temperature and decrease the volume fraction of primary Cu_6Sn_5, additional experiments were performed on Sn-2Cu (which has a lower liquidus, and forms a lower fraction of Cu_6Sn_5 than Sn-4Cu) to compare Cu_6Sn_5 grain size in Sn-2Cu, Sn-4Cu and Sn-4Cu-Al solders.

Alloys containing 0-0.2wt%Al were prepared by mixing 99.9 Sn, and Sn-10Cu and Sn-1Al master alloys in a graphite crucible and heating to 450°C in a resistance furnace. Once liquid, the alloys were stirred and held at 450°C for 60 mins before the liquid was drawn with vacuum

into borosilicate glass tubes with inner diameter 4mm. The resulting rods were then cut into samples.

DSC experiments were performed for thermal analysis of Cu_6Sn_5 nucleation. A Mettler Toledo DSC was used at 5 K/min to test 200 mg samples in Al_2O_3 pans under a N_2 atmosphere. Cyclic DSC was used to identify the equilibrium Cu_6Sn_5 liquidus temperature because the liquidus temperature could not be identified reliably from a standard heating curve due to the small heat flux associated with primary Cu_6Sn_5 melting. This is because the combination of the steep Cu_6Sn_5 liquidus slope and the low mass fraction of Cu_6Sn_5, absorbs only a small amount of heat over a wide temperature range (e.g. in Sn-4Cu, ~8.1 mass% Cu_6Sn_5 forms over a ~122 K temperature interval [19]). The cyclic DSC method used was similar to that in previous studies on hypereutectic solder compositions [20] and on superalloys [21].

The procedure of cyclic DSC is outlined in Figure 1(a) for a Sn-4Cu-0.02Al sample. The system was heated at 5K/min to a temperature where a mixture of liquid and Cu_6Sn_5 is known to exist, and was then held isothermally for 30 minutes. The system was then heated at 5 K/min to 400°C and cooled at 5K/min to 305°C, ending the first circle. The next cycle involved isothermal holding at a temperature 2.5K higher than the previous cycle, and subsequent cycles raised the isothermal holding temperature by a further 2.5K in each cycle. Figure 1(a) shows six cycles.

If an endothermic peak was detectable during heating after isothermal holding, some primary Cu_6Sn_5 was present at the prior isothermal holding temperature which was defined as being below the liquidus temperature. When no endothermic peak was found on heating after isothermal holding, the sample had completely melted at the prior isothermal holding temperature, which was defined as being above the liquidus temperature. The liquidus temperature is between the maximum Cu_6Sn_5+L temperature and minimum fully liquid

temperature, and the median value of the two was taken as the measured liquidus temperature with an error of plus/minus half an interval, 1.25K. The nucleation undercooling was then defined as the measured Cu_6Sn_5 liquidus temperature determined by cyclic DSC minus the Cu_6Sn_5 onset on cooling (Figure 1(b)).

To generate microstructures at a cooling rate relevant to soldering, samples were cooled at ~1.7 K/s in quartz tubes. Two tubes each containing a 500±0.5 mg sample were fixed at the fan level in the centre of a forced air convection oven. The oven was heated to 450°C and a BN-coated 0.5 mm K-type thermocouple was inserted at the centre of one sample. After 30 mins at 450°C, the oven door was opened generating a cooling rate of 1.68±0.10 K/s in the liquid prior to the nucleation of Cu_6Sn_5. The sample without a thermocouple was used for microstructural analysis.

Samples were mounted in Struers VersoCit acrylic cold mounting resin and wet ground to 2400 grit with SiC paper followed by polishing with colloidal silica on a nap cloth for 6 mins. Cross-sections were investigated using a Zeiss Auriga field emission gun scanning electron microscope (FEG-SEM), equipped with an Oxford Instruments INCA 80mm^2 x-sight energy dispersive X-ray (EDX) detector and Oxford Instruments Nordlys S electron backscatter diffraction (EBSD) detector.

HKL Flamenco acquisition software was used to index Kikuchi patterns and phases were identified by combining EBSD and EDX. Orientation relationships were determined by indexing and analysing pairs of EBSD patterns obtained from particles sharing a common interface.

The primary Cu_6Sn_5 grain size was measured from EBSD maps with area equal to 2mm x 1.5mm. Two techniques were applied depending on the intricacy of the Cu_6Sn_5 microstructure. For Al-containing microstructures, a 4µm by 4 µm step size was used to scan the whole area.

For Sn-Cu samples, line-scan mapping was used with 4 μm step size and 10 μm line spacing to improve time efficiency of assessing these microstructures, as microstructural features in Sn-4Cu microstructures usually spanned a larger area than in Al-containing samples. Post analysis of EBSD maps extrapolated the indexed points to all pixels of Cu_6Sn_5 by defining all pixels within a contiguous region of Cu_6Sn_5 (identified in secondary electron images) as having the same orientation. The scope of this analysis is to identify common Cu_6Sn_5 grains within the βSn matrix, where the Cu_6Sn_5 grains are intricate 3D structures that are only sampled within 2D cross sections.

For the investigation of the three-dimensional morphology of intermetallics, some samples were etched in a solution of 5% NaOH and 3.5% orthonitrophenol in distilled H_2O at 60 °C for approximately 15 min to selectively remove the matrix βSn. Single crystal intermetallics were then placed on a stub and studied with secondary electron imaging in the SEM.

3. Results

3.1 Influence of Al on nucleation undercooling of Cu_6Sn_5

Table 2 and Figure 1(b-c) summarise the DSC data on the nucleation of Cu_6Sn_5 in Sn-4Cu-xAl alloys, and Figure 1 (c) plots the nucleation undercooling versus Al content. It can be seen that the nucleation undercooling for Cu_6Sn_5 decreases with increasing Al content and, therefore, that Al additions lower the nucleation barrier for Cu_6Sn_5.

From Table 2 and Figure 1(b-c), the Cu_6Sn_5 nucleation temperature was relatively constant with a standard deviation of only ±0.22K or less, even in binary Sn-4Cu. Note that the error bar in Figure 1(b) is mostly due to the uncertainty in the Cu_6Sn_5 liquidus temperature measurement.

Reproducibility in the Cu_6Sn_5 nucleation temperature is in marked contrast to the variable nucleation temperature typical of the βSn phase in most solders [22-24]. It is also notable that no additional heat flux peaks were detected in Al-containing samples over the temperature range studied.

3.2 Influence of Al on Cu_6Sn_5 microstructure

The influence of Al additions on the Cu_6Sn_5 grain structure is summarised in Figures 2 and 3. Figure 2 (a-c) are whole-sample 2D sections where primary Cu_6Sn_5 grains are bright and the βSn-Cu_6Sn_5 eutectic is dark. The Cu_6Sn_5 grains appear as numerous discrete regions and it is not possible to reliably measure how many Cu_6Sn_5 grains are in each cross-section from these optical micrographs. Figure 2 (d-e) are SE-SEM images of typical extracted Cu_6Sn_5 grains after selective etching of the βSn showing that Cu_6Sn_5 have a complex branched structure in 3D and that the Cu_6Sn_5 grains are significantly more branched in Sn-4Cu than in Sn-4Cu-0.2Al. In comparing the size of the typical Cu_6Sn_5 grains in Figure 2(d-e), note that the Cu_6Sn_5 grain in Sn-4Cu (Figure 2(d)) is only a fragment of one grain (the fracture surface is the top of the grain in Figure 2(d)) whereas the Cu_6Sn_5 grain in Sn-4Cu-0.2Al (Figure 2(e)) is a complete grain, and that the true size of typical Cu_6Sn_5 grains in Sn-4Cu is significantly larger than in Sn-4Cu-0.2Al.

Due to the complex and non-equiaxed shape of Cu_6Sn_5 grains (Figure 2(d-e)), there is no simple definition of 'grain size' for the Cu_6Sn_5 grains, and it is more meaningful to measure the number of Cu_6Sn_5 grains per unit area from EBSD orientation maps. This measurement is directly related to the number of Cu_6Sn_5 grains per unit volume [25] and, therefore, to the number of nucleation events per unit volume.

Figure 3(a-c) are BSE-SEM images of typical ~2mm x 1.5mm areas in Sn-2Cu, Sn-4Cu and Sn-4Cu-0.2Al. Figure 3(d-f) are extrapolated EBSD maps of the same regions, where each colour represents a single Cu_6Sn_5 grain orientation and black regions were either indexed as βSn or were eutectic Cu_6Sn_5 that were not indexed with the mapping settings used. In binary Sn-4Cu, numerous discrete Cu_6Sn_5 regions in the BSE image of Figure 3 (b) can be seen to belong to only 17 Cu_6Sn_5 grains in the EBSD map of Figure 3 (e). In contrast, in Sn-4Cu-0.2Al, the discrete Cu_6Sn_5 regions in the BSE image of Figure 3 (c) are ~173 Cu_6Sn_5 grains in the EBSD map of Figure 3 (f). Thus, the Al addition has caused significant Cu_6Sn_5 grain refinement.

The influence of Al on the nucleation of Cu_6Sn_5 is quantified in Figure 3 (g) from four EBSD maps of ~2mm x 1.5mm each in each composition. In Sn-4Cu-0.2Al, the number of Cu_6Sn_5 grains per unit area increases by a factor of ~7.8 comparing with Sn-4Cu. That is to say, the Al addition increased the number of Cu_6Sn_5 grains per unit area by a factor of ~8.

Another influence of the Al addition was to reduce the volume fraction of Cu_6Sn_5. This is quantified in Figure 3(h) where Sn-4Cu contains ~10.5 vol% Cu_6Sn_5 and Sn-4Cu-0.2Al contains ~9.2 vol% Cu_6Sn_5. Experiments on Sn-2Cu confirm that a reduction in volume fraction of Cu_6Sn_5 does not significantly influence Cu_6Sn_5 nucleation since Sn-2Cu has an even lower volume fraction of primary Cu_6Sn_5 than Sn-4Cu-0.2Al (see Figure 3(h)) and yet the number of Cu_6Sn_5 grains per unit area in Sn-2Cu is similar to that in Sn-4Cu and much lower than in Sn-4Cu-0.2Al (see Figure 3(a-g)).

3.3 Identification of heterogeneous nuclei

There were commonly Cu_xAl_y particles near the centre of Cu_6Sn_5 grains in Sn-4Cu-0.02Al and Sn-4Cu-0.2Al, which are likely to be the heterogeneous nuclei involved in grain refinement. These were found to take a variety of morphologies and a representative spectrum of shapes is shown in Figure 4. Figure 4 (a) shows numerous Cu_xAl_y particles clustered around the lower part of a Cu_6Sn_5 grain. Figure 4 (b) is a section through a similar area where some Cu_xAl_y particles are within the Cu_6Sn_5 grain and others are attached to the outside. All Cu_xAl_y particles in Figure 4 (a) and (b) are rounded and only weakly-faceted. In contrast, Figure 4 (c-f) show highly faceted Cu_xAl_y particles near the centre of Cu_6Sn_5 grains where the Cu_xAl_y either have a simple polygonal shape or are branched.

Figure 5 reveals 3D morphologies of typical faceted Cu_xAl_y particles after selective etching of βSn. The grains have undergone an increasing growth distance from (a) → (d), as the magnification decreases from (a) to (d). Many of the smallest Cu_xAl_y particles were near-cuboidal, similar to Figure 5 (a). Larger grains commonly had depressions near their facet centres, similar to Figure 5 (b), most likely due to slower growth in facet centres and faster growth at edges and corners where solute diffusion is more effective at preventing solute build-up. This growth instability then promotes hopper crystals, which were commonly observed (e.g. Figure 5 (c)). The largest Cu_xAl_y particles were usually faceted dendritic, e.g. in Figure 5 (d), which probably formed because the continued growth of hopper crystals occurred fastest at the corners. The 3D shapes in Figure 5 can be used to interpret the 2D sections in Figure 4. The Cu_xAl_y particles in Figure 4 (e-f) are most likely sections through a hopper crystal (Figure 5 (c)) or faceted-dendritic crystal (Figure 5 (d)). In Figure 5(e), an example of a Cu_6Sn_5 grain growing from a Cu_xAl_y grain is shown where the Cu_6Sn_5 grain appears to have nucleated from the lower part of the ‘Y’ shape in this case.

In order to identify the Cu_xAl_y phase(s), SEM-EDX was coupled with EBSD. EDX data from 21 particles gave a mean composition of Al-64at%Cu with a standard deviation of ±0.9 at%, and there was negligible Sn (the mean measured Sn content was below the detection limits of EDX). No systematic variation in composition was found between Cu_xAl_y particles with different morphologies (i.e. weakly-faceted, round, faceted-polygonal or faceted-dendritic particles such as those in Figure 4).

Examining the most recent Al-Cu phase diagram [26], we note that Al-64%Cu (±0.9 at%) is between the δ-$Cu_{33}Al_{17}$ and γ_1-Cu_9Al_4 phases. The crystal structures of these phases are summarised in Table 3 [27-30]. EBSD analysis of >17 Cu_xAl_y particles was performed with these parameters. It was found that both model structures (δ-$Cu_{33}Al_{17}$ and γ_1-Cu_9Al_4) could be well-fit to the experimental EBSD patterns. The analysis involved comparing the detected bands with the potential reflectors predicted by the kinematical structure factor analysis, using the mean angular deviation (MAD) in HKL Channel 5 and EDAX TSL OIM software, and visual inspection band-by-band. A low MAD of <0.44 was found in each case using the eight bands of highest intensity and a suitable pattern centre calibration on the neighbouring tin phase and visual inspection of indexed patterns confirmed the good fit of both. Further Figures on the fitting of both phases are shown in Supplementary Information Part 1.

Examination of the δ-$Cu_{33}Al_{17}$ and γ_1-Cu_9Al_4 crystal structures shows why both model structures are an excellent fit to the EBSD patterns and why EBSD was not able to discriminate between the phases by this method: γ_1-Cu_9Al_4 is the prototype primitive-cubic gamma brass [30] and δ-$Cu_{33}Al_{17}$ is a rhombohedral gamma brass [29] with angle $\alpha=\beta=\gamma=89.74°$ that is very close to cubic and with similar lattice parameters and atomic positions to the γ_1-Cu_9Al_4 phase [30] (Table 3). To highlight the similarity between the phases, Figure 6 is a projection view along [100] in γ_1-

Cu_9Al_4 and δ-$Cu_{33}Al_{17}$ where it can be seen that there are only slight deviations in the atom positions.

We proceed by first assuming that the nucleant phase is γ_1-Cu_9Al_4 and then, towards the end of the results section, we reanalyse our data assuming the nucleant phase is δ-$Cu_{33}Al_{17}$. It will become clear that both δ-$Cu_{33}Al_{17}$ and γ_1-Cu_9Al_4 are predicted to be highly potent nuclei.

3.4 Identification of the orientation relationships of nucleation

In many cases there was a clear relationship between the orientation of the facets of the Cu_xAl_y particle and the surrounding Cu_6Sn_5 grain. For example, in Figure 4 (c), the facets of both Cu_xAl_y and Cu_6Sn_5 are near-parallel, while in Figure 4 (d,f) the facets of Cu_xAl_y are near-parallel with the diagonal through two second nearest neighbouring corners of the Cu_6Sn_5 grain (as indicated with dotted lines in Figure 4). Therefore, these interfacial planes and orientation relationships were studied by ESBD.

EBSD studies on η-Cu_6Sn_5 grains extracted after dissolution of the βSn matrix confirmed that the main growth facets of η-Cu_6Sn_5 in Sn-4Cu-0.2Al are the first order prism planes (i.e. $\{1\bar{1}00\}$) as shown in Figure 7.

Figure 8 (A-C) demonstrates a typical Cu_xAl_y particle near the centre of a Cu_6Sn_5 grain and corresponding EBSD patterns from each phase. Comparing the EBSD patterns of (B) Cu_6Sn_5 and (C) Cu_xAl_y clearly shows that there are various parallel planes (indicated with overlapping of the respective Kikuchi bands in the diffraction patterns). In Figure 8(b_1) Cu_6Sn_5 has been indexed to hexagonal η-Cu_6Sn_5 [27] (Table 3) because this phase is expected to have been present at T>186°C prior to superstructure ordering at lower temperature [4]. In Figure 8, Cu_xAl_y

has been indexed to cubic γ_1-Cu_9Al_4 [30] and the unit cell orientations are given in the wireframe inserts to (b_1-c_2). The orientation relationship can be written:

$(1\bar{1}00)_{Cu6Sn5}||(2\bar{1}\bar{1})_{Cu9Al4}$ and $[0001]_{Cu6Sn5}$ || $[111]_{Cu9Al4}$.

This OR was measured for 17 pairs of Cu_xAl_y/η-Cu_6Sn_5 grains (more examples are available in Supplementary Information Part 2). The data are summarised in a stereographic projection in Figure 9 with respect to [111] of γ_1-Cu_9Al_4. Figure 9(a) shows all measured orientations rotated towards one representative orientation (via exploiting symmetry). It can be seen that the [111] direction in γ_1-Cu_9Al_4 is within 2.64±0.63° of [0001] in η-Cu_6Sn_5, while the projections of $(10\bar{1})$ in γ_1-Cu_9Al_4 are within 2.30±1.02° of the $(1\bar{2}10)$ reference plane in η-Cu_6Sn_5. Uncertainty has been calculated here using the average of the angles between the two lattices measured with EBSD.

The nucleation interfaces (i.e. habit planes) in this OR, can be inferred by comparing the orientation of the $\{1\bar{1}00\}$ growth facets of η-Cu_6Sn_5 with the η-Cu_6Sn_5-Cu_xAl_y interfaces. The common observation of the facets of Cu_xAl_y and Cu_6Sn_5 being near-parallel (e.g. Figures 4 (c) and 8(A)) is consistent with $(1\bar{1}00)_{Cu6Sn5}$ being a nucleation interface. Additionally, the often-observed facets of Cu_xAl_y near-parallel with the diagonal through two second nearest neighbouring corners of the Cu_6Sn_5 grain (see dotted lines in Figure 4(d) and (f)) is consistent with $(1\bar{2}10)_{Cu6Sn5}$ being a nucleation interface. Therefore, the OR and its two possible interfacial planes can be summarised as:

$(1\bar{2}10)_{Cu6Sn5}||(10\bar{1})_{Cu9Al4}$ and $[0001]_{Cu6Sn5}$ || $[111]_{Cu9Al4}$ with interfacial plane being either $(1\bar{1}00)_{Cu6Sn5}||(2\bar{1}\bar{1})_{Cu9Al4}$ or $(1\bar{2}10)_{Cu6Sn5}||(10\bar{1})_{Cu9Al4}$.

These interfacial planes and common directions are highlighted with black lines in the indexed EBSD patterns in Figure 8 (b_1,c_1) and Figure 8 (b_2,c_2).

Next, we reanalyse the 17 pairs of EBSD patterns indexing the Cu_xAl_y particles as δ-$Cu_{33}Al_{17}$. Among the 17 pairs of δ-$Cu_{33}Al_{17}$/η-Cu_6Sn_5 grains, 7 pairs show the same OR as when indexing to γ_1-Cu_9Al_4:

$(1\bar{2}10)_{Cu6Sn5}$ || $(10\bar{1})_{Cu33Al17}$ and $[0001]_{Cu6Sn5}$ || $[111]_{Cu33Al17}$ with interfacial plane as $(1\bar{1}00)_{Cu6Sn5}$||$(2\bar{1}\bar{1})_{Cu33Al17}$ or $(1\bar{2}10)_{Cu6Sn5}$||$(10\bar{1})_{Cu33Al17}$.

Note that this OR can be written also in terms of the hexagonal supercell of δ-$Cu_{33}Al_{17}$ (i.e. hR156 in Table 3) in which case the hexagonal cells of η-Cu_6Sn_5 and δ-$Cu_{33}Al_{17}$ are simply related by:

$(1\bar{2}10)_{Cu6Sn5}$ || $(1\bar{2}10)_{Cu33Al17}$ and $[0001]_{Cu6Sn5}$ || $[0001]_{Cu33Al17}$ with interfacial plane as $(1\bar{1}00)_{Cu6Sn5}$||$(1\bar{1}00)_{Cu33Al17}$ or $(1\bar{2}10)_{Cu6Sn5}$||$(1\bar{2}10)_{Cu33Al17}$.

The remaining 10 pairs exhibited a second OR because rhombohedral δ-$Cu_{33}Al_{17}$ is slightly distorted along [111]. Although this distortion is extremely small as the lattice angle of rhombohedral δ-$Cu_{33}Al_{17}$ is marginally less than 90 degree (Table 3), the symmetry of the crystal structure is changed and therefore <111> is different from <$1\bar{1}1$>. The OR_2 can then be summarised as:

$(1\bar{2}10)_{Cu6Sn5}$ || $(10\bar{1})_{Cu33Al17}$ and $[0001]_{Cu6Sn5}$ || $[1\bar{1}1]_{Cu33Al17}$ with interfacial plane $(1\bar{2}10)_{Cu6Sn5}$ || $(10\bar{1})_{Cu33Al17}$.

Or, in terms of the hexagonal supercell of δ-$Cu_{33}Al_{17}$:

$(1\bar{2}10)_{Cu6Sn5}$ || $(1\bar{2}10)_{Cu33Al17}$ and $[0001]_{Cu6Sn5}$ || $[\bar{2}021]_{Cu33Al17}$ with interfacial plane as $(1\bar{2}10)_{Cu6Sn5}$ || $(1\bar{2}10)_{Cu33Al17}$.

Figure 9(b) shows the stereographic projection of the OR_2, note that the [0001] of Cu_6Sn_5 is within 1.68±0.51° of the $[1\bar{1}1]$ direction in δ-$Cu_{33}Al_{17}$, while the projection of $(1\bar{2}10)$ in η-Cu_6Sn_5 are within 1.05±0.83° of $(10\bar{1})$ in δ-$Cu_{33}Al_{17}$.

4. Discussion

4.1 Grain refinement

Figure 3(g) shows that the 0.2wt%Al addition increased the number of Cu_6Sn_5 grains per unit area by a factor of 8, which indicates a large increase in Cu_6Sn_5 nucleation events. This significant increase in Cu_6Sn_5 grains per unit area did not result in equiaxed Cu_6Sn_5 grains as is common of the grain refinement in casting alloys [31, 32]. Instead, increased nucleation resulted in numerous Cu_6Sn_5 grains elongated along the [0001] direction and with $\{1\bar{1}00\}$ growth facets (Figures 2(e), 5(e) and 7), which is a result of the anisotropic attachment kinetics associated with the free growth of faceted crystals. The increased nucleation can be understood from the grain refinement theories developed for structural casting alloys that stress the importance of both numerous potent nuclei and growth restricting solute in obtaining a small grain size during solidification (e.g. [31]).

4.2 Nucleant potency

Nucleant potency is determined by the degree of lattice matching across the solid-nucleant interface; the better the match the higher the nucleant potency. A good lattice match allows a coherent or partially coherent interface to form, and the better the match the lower the strain energy at the interface and the lower the interfacial energy [33]. In many systems the lattice match associated with potent nuclei is relatively simple; for example, between two phases that have the same crystal structure and similar lattice parameters (e.g. AlP and Si [34] or Zr and Mg

[32]). In the present case, the lattice match associated with heterogeneous nucleation is more complex with interfacial planes containing zig-zag rows in the δ-$Cu_{33}Al_{17}$ and/or γ_1-Cu_9Al_4 nuclei and straight rows in η-Cu_6Sn_5 and with partially-occupied sites in δ-$Cu_{33}Al_{17}$ and η-Cu_6Sn_5. In such a case, a useful model to identify low energy interfaces is the edge-to-edge matching model [33]. This predicts that a potent nucleation interface will involve the closest packed rows in the two crystals meeting edge to edge in the habit plane, with small mismatch (<5-10%) within these rows and small mismatch (<5-10%) between the rows. These conditions are met in the experimentally determined ORs as can be seen in the 3D representation in Figure 10. The closest-packed directions are [0001] in η-Cu_6Sn_5 and [111] in γ_1-Cu_9Al_4 and the closest-packed planes are $(1\bar{2}10)$ in η-Cu_6Sn_5 (highlighted yellow) and $(10\bar{1})$ in γ_1-Cu_9Al_4 (highlighted red). Figure 10 (a-b) show the OR and two interfacial planes (marked by black and red shaded planes). Note that both interfacial planes contain the closest-packed directions meeting edge-to-edge. It can be seen that the atomic spacings along the closest-packed directions $[0001]_{Cu6Sn5}$ || $[111]_{Cu9Al4}$ have 0.8% misfit and d-spacings of the closest-packed planes $(1\bar{2}10)_{Cu6Sn5}$ || $(10\bar{1})_{Cu9Al4}$ have 2.8% misfit, consistent with a highly potent nucleant [35]. A similar lattice matching analysis using δ-$Cu_{33}Al_{17}$ and Cu_6Sn_5 can be found in Supplementary Information Part 3 which shows that the lattice match and atomic configuration in the interfacial planes is very similar for this OR in δ-$Cu_{33}Al_{17}$ || Cu_6Sn_5 and γ_1-Cu_9Al_4 || Cu_6Sn_5. In particular, the mismatch within the close packed rows is 1.3% and the mismatch between the d-spacing of close-packed planes is 3.3%.

Another model of lattice matching is Bramfitt's planar lattice matching [36]. The planar lattice match of these interfacial planes are shown in Figure 10 (c-d). Note that the colours correspond to the shaded planes in Figure 10 (a-b). For γ_1-Cu_9Al_4, zigzag atoms have been projected onto the interfacial planes and are denoted by open symbols. For η-Cu_6Sn_5, the interfacial planes are

flat and the atoms are denoted by solid symbols (fully occupied) or half-solid symbols (20% occupied Cu). In Figure 10 (c), the lattice misfit along $[0001]_{Cu6Sn5}$ || $[111]_{Cu9Al4}$ is 0.8% while the lattice misfit along $[\bar{1}2\bar{1}0]_{Cu6Sn5}$ || $[10\bar{1}]_{Cu9Al4}$ is 2.8%. In Figure 10 (d), the lattice misfit along $[0001]_{Cu6Sn5}$ || $[111]_{Cu9Al4}$ is also 0.8% and the lattice misfit along $[\bar{1}100]$ || $[11\bar{2}]$ is 3.2%. The planar disregistry between Cu_6Sn_5 and Cu_9Al_4/$Cu_{33}Al_{17}$ are quantified in Table 4. The disregistry is less than 2.5% in each case and the match is marginally better between η-Cu_6Sn_5 and γ_1-Cu_9Al_4 than between η-Cu_6Sn_5 and δ-$Cu_{33}Al_{17}$. The overall misfit of ~2.5% in each case is comparable to well-known potent nuclei, such as TiN for δFe [36], Zr for αMg [32], and Al_3Ti for αAl [37]. This value is also similar to the lattice mismatch associated with nucleation of metastable $NiSn_4$ on impurity $FeSn_2$ in solders [38].

Theoretical lattice matching predicts that δ-$Cu_{33}Al_{17}$ and γ_1-Cu_9Al_4 provide an almost equally good lattice match to Cu_6Sn_5, and both are predicted to be potent nuclei for Cu_6Sn_5. Therefore, it is likely that good grain refinement can be achieved with either δ-$Cu_{33}Al_{17}$ and γ_1-Cu_9Al_4.

4.3 Growth restriction

The role of solute in grain refinement is (i) to restrict crystal growth due to the build-up of solute at interfaces which requires the interface to cool down as it grows [39] and (ii) to cause the development of constitutionally supercooled regions in the liquid in which further nucleation events can occur [40]. The extent to which solute restricts growth is often quantified via the 'growth restriction factor', Q, which for binary phase diagrams that are well-approximated as having a linear liquidus slope and constant partition coefficient, is given by Eq. 1 [31, 39]:

$$Q = C_0 m_l (k-1) \quad \text{Eq. 1}$$

Where C_0 is the bulk alloy composition, m_l is the liquidus slope and k is the partition coefficient. Since neither k nor m_l are constants for hypereutectic Sn-Cu alloys, it is more convenient to find Q from the development of solute undercooling with solid fraction in the early stages of solidification from Eq. 2 (e.g. [41, 42]).

$$Q = \left(\frac{d(\Delta T_s)}{df_s}\right)_{f_s \to 0} \qquad \text{Eq. 2}$$

Where f_s is the solid fraction, ΔT_s is the solutal undercooling at the Cu_6Sn_5-liquid interface defined as $T_L - T^*$ with T_L being the liquidus temperature and T^* the Cu_6Sn_5-liquid interface temperature. Figure 11 plots ΔT_s versus f_s using phase diagram data from [19]. The derivative as f_s approaches zero is also plotted on Figure 11, yielding a value of $Q = 839\ K$. The value of $Q = 839\ K$ is large and much larger than typical values for solute rejection during primary phase growth in Al, Mg and Ti alloy solidification [31, 32, 43]. Thus, the rejection of Sn at Cu_6Sn_5-liquid interfaces will cause strong growth restriction of Cu_6Sn_5 and significant constitutional supercooling in the liquid ahead of interfaces.

Since Q is so large in binary Sn-4Cu, it is unlikely that grain refinement by Al additions is related to a further increase in the growth restriction factor. Instead, the naturally high growth restriction factor of Sn-4Cu generates significant constitutional supercooling in which the potent nulcei (i.e. γ_1-Cu_9Al_4 and/or δ-$Cu_{33}Al_{17}$) can trigger further nucleation events and create a high number density of Cu_6Sn_5 grains.

5. Conclusions

This work has revealed the mechanisms of Cu_6Sn_5 grain refinement in Sn-Cu solders with dilute Al additions. A DSC and analytical SEM study has found the following:

(i) A 0.2wt%Al addition decreased the nucleation undercooling of Cu_6Sn_5 from 7.8 to 3.6K and increased the number of Cu_6Sn_5 grains per unit area by a factor of ~8.

(ii) Many Cu_6Sn_5 particles contained a Cu_xAl_y particle near their centre. This phase was identified as either γ_1-Cu_9Al_4 or δ-$Cu_{33}Al_{17}$ by combining EDS with EBSD. An EBSD study of orientation relationships and an analysis of the crystallography in the interfacial planes showed that both δ-$Cu_{33}Al_{17}$ and γ_1-Cu_9Al_4 give an equally good lattice match to η-Cu_6Sn_5.

(iii) For γ_1-Cu_9Al_4, one common OR and two nucleation interfaces were identified, each with planar lattice disregistry of less than 2.5%:

$(1\bar{2}10)_{\mathrm{Cu6Sn5}}||(10\bar{1})_{\mathrm{Cu9Al4}}$ and $[0001]_{\mathrm{Cu6Sn5}}||[111]_{\mathrm{Cu9Al4}}$ with either $(1\bar{1}00)_{\mathrm{Cu6Sn5}}||(2\bar{1}\bar{1})_{\mathrm{Cu9Al4}}$ or $(1\bar{2}10)_{\mathrm{Cu6Sn5}}||(10\bar{1})_{\mathrm{Cu9Al4}}$ as the interfacial plane.

(iv) For δ-$Cu_{33}Al_{17}$, one OR is exactly the same as that of γ_1-Cu_9Al_4:

$(1\bar{2}10)_{\mathrm{Cu6Sn5}}$ || $(10\bar{1})_{\mathrm{Cu33Al17}}$ and $[0001]_{\mathrm{Cu6Sn5}}$ || $[111]_{\mathrm{Cu33Al17}}$ with interfacial plane being either $(1\bar{1}00)_{\mathrm{Cu6Sn5}}||(2\bar{1}\bar{1})_{\mathrm{Cu33Al17}}$ or $(1\bar{2}10)_{\mathrm{Cu6Sn5}}||(10\bar{1})_{\mathrm{Cu33Al17}}$.

The other OR is due to the distortion in δ-$Cu_{33}Al_{17}$, where <111> is different from $<1\bar{1}1>$:

$(1\bar{2}10)_{\mathrm{Cu6Sn5}}$ || $(10\bar{1})_{\mathrm{Cu33Al17}}$ and $[0001]_{Cu6Sn5}$ || $[1\bar{1}1]_{Cu33Al17}$ with $(1\bar{2}10)_{\mathrm{Cu6Sn5}}$ || $(10\bar{1})_{\mathrm{Cu33Al17}}$ as the interfacial plane.

(v) An analysis of the growth restriction factor (GRF) in binary Sn-4Cu shows that solute rejection strongly restricts growth for this composition and that a large degree of constitutional supercooling develops in the liquid. Therefore, hyper-eutectic Sn-Cu alloys are responsive to grain refinement by the addition of potent heterogeneous nuclei which become activated in the supercooled liquid.

The results show that dilute Al additions to hypereutectic Sn-Cu alloys cause strong grain refinement of primary Cu_6Sn_5 due to the introduction of potent heterogeneous nuclei to an alloy with inherently high growth restriction factor.

References

[1] I.E. Anderson, J.W. Walleser, J.L. Harringa, F. Laabs, A. Kracher, Nucleation Control and Thermal Aging Resistance of Near-Eutectic Sn-Ag-Cu-X Solder Joints by Alloy Design, J. Electron. Mater., 38 (2009) 2770-2779.
[2] G. Zeng, S.D. McDonald, J. Read, Q. Gu, K. Nogita, Kinetics of the polymorphic phase transformation of Cu6Sn5, Acta Mater., 69 (2014) 135-148.
[3] U. Schwingenschlogl, C. Di Paola, K. Nogita, C.M. Gourlay, The influence of Ni additions on the relative stability of eta and eta(') Cu6Sn5, Appl. Phys. Lett., 96 (2010).
[4] K. Nogita, C.M. Gourlay, S.D. McDonald, Y.Q. Wu, J. Read, Q.F. Gu, Kinetics of the η-η' transformation in Cu_6Sn_5, Scripta Mater., 65 (2011) 922-925.
[5] H.R. Kotadia, O. Mokhtari, M. Bottrill, M.P. Clode, M.A. Green, S.H. Mannan, Reactions of Sn-3.5Ag-Based Solders Containing Zn and Al Additions on Cu and Ni(P) Substrates, J. Electron. Mater., 39 (2010) 2720-2731.
[6] A. Kantarcıoğlu, Y.E. Kalay, Effects of Al and Fe additions on microstructure and mechanical properties of SnAgCu eutectic lead-free solders, Mater. Sci. Eng. A, 593 (2014) 79-84.
[7] Y.K. Jee, X. Yang-hua, Y. Jin, K. Hyun-Woo, L. Taek-Young, Effect of Al addition in Sn-Ag solder on the interfacial reactions with Cu and ENIG metallizations, in: Electronic Components and Technology Conference, 2008. ECTC 2008. 58th, 2008, pp. 491-494.
[8] H.R. Kotadia, A. Panneerselvam, O. Mokhtari, M.A. Green, S.H. Mannan, Massive spalling of Cu-Zn and Cu-Al intermetallic compounds at the interface between solders and Cu substrate during liquid state reaction, J. Appl. Phys., 111 (2012).
[9] F. Somidin, M.A.A.M. Salleh, K.R. Ahmad, Intermetallic Compound Formation on Solder Alloy/Cu-Substrate Interface Using Lead-Free Sn-0.7Cu/Recycled-Aluminum Composite Solder, Adv. Mater. Res., 620 (2012) 105-111
[10] S. McDonald, K. Nogita, J. Read, T. Ventura, T. Nishimura, Influence of Composition on the Morphology of Primary Cu_6Sn_5 in Sn-4Cu Alloys, J. Electron. Mater., 42 (2013) 256-262.
[11] Y.H. Xia, Y.K. Jee, J. Yu, T.Y. Lee, Effect of Aluminum Concentration on the Interfacial Reactions of Sn-3.0Ag-xAl Solders with Copper and ENIG Metallizations, J. Electron. Mater., 37 (2008) 1858-1862.
[12] M.F.M. Sabri, D.A. Shnawah, I.A. Badruddin, S.B.M. Said, F.X. Che, T. Ariga, Microstructural stability of Sn–1Ag–0.5Cu–xAl (x=1, 1.5, and 2wt.%) solder alloys and the effects of high-temperature aging on their mechanical properties, Mater. Charact., 78 (2013) 129-143.
[13] M.F.M. Sabri, D.A. Shnawah, I.A. Badruddin, S.B.M. Said, Effects of aging on Sn–1Ag–0.5Cu solder alloys containing 0.1wt.% and 0.5wt.% Al, J. Alloys Compd., 582 (2014) 437-446.

[14] D.-A. Shnawah, M. Sabri, I. Badruddin, S. Said, F. Che, The bulk alloy microstructure and mechanical properties of Sn–1Ag–0.5Cu–xAl solders (x = 0, 0.1 and 0.2 wt. %), J. Mater. Sci.: Mater. Electron., 23 (2012) 1988-1997.
[15] D.-A. Shnawah, S. Said, M. Sabri, I. Badruddin, T. Hoe, F. Che, A. Abood, Microstructure and Tensile Properties of Sn-1Ag-0.5Cu Solder Alloy Bearing Al for Electronics Applications, J. Electron. Mater., 41 (2012) 2073-2082.
[16] B. Huang, H.S. Hwang, N.C. Lee, A Compliant and Creep Resistant SAC-Al(Ni) Alloy, in: Electronic Components and Technology Conference, 2007. ECTC '07. Proceedings. 57th, 2007, pp. 184-191.
[17] A.J. Boesenberg, I.E. Anderson, J.L. Harringa, Development of Sn-Ag-Cu-X Solders for Electronic Assembly by Micro-Alloying with Al, J. Electron. Mater., 41 (2012) 1868-1881.
[18] J.F. Li, P.A. Agyakwa, C.M. Johnson, Effect of trace Al on growth rates of intermetallic compound layers between Sn-based solders and Cu substrate, J. Alloys Compd., 545 (2012) 70-79.
[19] Thermo-Calc, NIST Solder Solutions Database version 1.0, in, 1999.
[20] K.W. Moon, W.J. Boettinger, U.R. Kattner, F.S. Biancaniello, C.A. Handwerker, Experimental and thermodynamic assessment of Sn-Ag-Cu solder alloys, J. Electron. Mater., 29 (2000) 1122-1136.
[21] R.I. Wu, J.H. Perepezko, Liquidus temperature determination in multicomponent alloys by thermal analysis, Metall. Mater. Trans. A, 31 (2000) 497-501.
[22] B. Arfaei, N. Kim, E.J. Cotts, Dependence of Sn Grain Morphology of Sn-Ag-Cu Solder on Solidification Temperature, J. Electron. Mater., 41 (2012) 362-374.
[23] S.A. Belyakov, C.M. Gourlay, Heterogeneous nucleation of βSn on NiSn4, PdSn4 and PtSn4, Acta Mater., 71 (2014) 56-68.
[24] B. Arfaei, M. Benedict, E.J. Cotts, Nucleation rates of Sn in undercooled Sn-Ag-Cu flip-chip solder joints, J. Appl. Phys., 114 (2013).
[25] J. Lelito, P.L. Zak, A.A. Shirzadi, A.L. Greer, W.K. Krajewski, J.S. Suchy, K. Haberl, P. Schumacher, Effect of SiC reinforcement particles on the grain density in a magnesium-based metal–matrix composite: Modelling and experiment, Acta Mater., 60 (2012) 2950-2958.
[26] N. Ponweiser, C.L. Lengauer, K.W. Richter, Re-investigation of phase equilibria in the system Al–Cu and structural analysis of the high-temperature phase η1-Al1−δCu, Intermetallics, 19 (2011) 1737-1746.
[27] K. Nogita, D. Mu, S.D. McDonald, J. Read, Y.Q. Wu, Effect of Ni on phase stability and thermal expansion of Cu_6–xNixSn$_5$ (x = 0, 0.5, 1, 1.5 and 2), Intermetallics, 26 (2012) 78-85.
[28] P. Villars, K. Cenzual, J. Daams, R. Gladyshevskii, O. Shcherban, V. Dubenskyy, V. Kuprysyuk, O. Pavlyuk, I. Savysyuk, S. Stoyko, $Cu_{31.27}(Cu_{0.57}Al_{0.43})_3Al_{16}$, Crystal Structures of Inorganic Compounds, 43A7 (2009) 285-286.
[29] E.H. Kisi, J.D. Browne, Ordering and structural vacancies in non-stoichiometric Cu-Al γ brasses, Acta Crystallogr. Sect. B, 47 (1991) 835-843.
[30] L. Arnberg, S. Westman, Crystal perfection in a noncentrosymmetric alloy. Refinement and test of twinning of the γ-Cu_9Al_4 structure, Acta Crystallogr. Sect. A, 34 (1978) 399-404.
[31] M. Easton, D. StJohn, Grain refinement of aluminum alloys: Part I. the nucleant and solute paradigms—a review of the literature, Metall. Mater. Trans. A, 30 (1999) 1613-1623.
[32] D.H. StJohn, M. Qian, M.A. Easton, P. Cao, Z. Hildebrand, Grain refinement of magnesium alloys, Metall. Mater. Trans. A, 36A (2005) 1669-1679.
[33] M.X. Zhang, P.M. Kelly, M.A. Easton, J.A. Taylor, Crystallographic study of grain refinement in aluminum alloys using the edge-to-edge matching model, Acta Mater., 53 (2005) 1427-1438.
[34] K. Nogita, S.D. McDonald, K. Tsujimoto, K. Yasuda, A.K. Dahle, Aluminium phosphide as a eutectic grain nucleus in hypoeutectic Al-Si alloys, J. Electron Microsc., 53 (2004) 361-369.

[35] P.M. Kelly, M.X. Zhang, Edge-to-edge matching—The fundamentals, Metall. Mater. Trans. A, 37 (2006) 833-839.
[36] B. Bramfitt, The effect of carbide and nitride additions on the heterogeneous nucleation behavior of liquid iron, Metall. Trans., 1 (1970) 1987-1995.
[37] P. Schumacher, A.L. Greer, J. Worth, P.V. Evans, M.A. Kearns, P. Fisher, A.H. Green, New studies of nucleation mechanisms in aluminium alloys: implications for grain refinement practice, Mater. Sci. Technol., 14 (1998) 394-404.
[38] S.A. Belyakov, C.M. Gourlay, Role of Fe impurities in the nucleation of metastable $NiSn_4$, Intermetallics, 37 (2013) 32-41.
[39] I. Maxwell, A. Hellawell, A simple model for grain refinement during solidification, Acta Metall., 23 (1975) 229-237.
[40] W. Winegard, B. Chalmers, Supercooling and dendritic freezing in alloys, Transactions of the ASM, 46 (1954) 1214-1223.
[41] T.E. Quested, A.T. Dinsdale, A.L. Greer, Thermodynamic modelling of growth-restriction effects in aluminium alloys, Acta Mater., 53 (2005) 1323-1334.
[42] R. Schmid-Fetzer, A. Kozlov, Thermodynamic aspects of grain growth restriction in multicomponent alloy solidification, Acta Mater., 59 (2011) 6133-6144.
[43] M.J. Bermingham, S.D. McDonald, M.S. Dargusch, D.H. StJohn, The mechanism of grain refinement of titanium by silicon, Scripta Mater., 58 (2008) 1050-1053.

Table 1. Summary of CuxAly phases in Al-containing solders reported in the literature.

Base solder [wt%]	Al addition [wt%]	Sub-strate	Cu_xAl_y phase	ref
Sn-0.7Cu	3.0-4.0	Cu	Cu_9Al_4	[9]
Sn-4.0Cu	0.025-0.2	-	*ND*	[10]
Sn-3.5Ag	0.5-2	Cu	$CuAl_2$ & *ND*	[5]
Sn-3Ag	0.1-1	Cu	$CuAl_2$	[11]
Sn-1Ag-0.5Cu	1.0-2.0	-	$CuAl_2$	[12]
Sn-1Ag-0.5Cu	0.1-0.5	-	CuAl	[13]
Sn-1Ag-0.5Cu	0.1-0.2	-	*ND*	[14]
Sn-1Ag-0.5Cu	0.1-0.5	-	*ND*	[15]
Sn-1Ag-0.5Cu	0.1-0.6	-	*ND*	[16]
Sn–3.5Ag–0.9Cu	0.05	Cu	*ND*	[6]
Sn-3.5Ag-0.95Cu	<0.25	Cu	$Cu_{33}Al_{17}$	[17]
Sn-3.8Ag-0.7Cu	1.0	-	CuAl	[18]
Sn-3.8Ag-0.7Cu	1.0	Cu	CuAl & $Cu_{33}Al_{17}$	[18]
Sn-3.8Ag-0.7Cu	2.0	Cu	$CuAl_2$	[8]

ND = Cu_xAl_y phase observed but not determined

Table 2. Summary of DSC data on liquidus temperature, nucleation temperature and nucleation undercooling for Cu_6Sn_5 in Sn-4Cu-xAl alloys.

	T_L (°C)	T_{nuc} (°C)	ΔT_{nuc} (°C)
Sn-4Cu	368.75±1.25	360.97±0.22	7.78±1.27
Sn-4Cu-0.02Al	346.25±1.25	340.18±0.05	6.07±1.25
Sn-4Cu-0.2Al	321.25±1.25	317.62±0.04	3.63±1.25

Table 3. Crystallographic data for η-Cu_6Sn_5, δ-$Cu_{33}Al_{17}$ and γ_1-Cu_9Al_4.

Phase	Pearson symbol	Space group	a [Å]	b [Å]	c [Å]	α [°]	β [°]	γ [°]	Ref
η-Cu_6Sn_5	*hP*4	*P*6_3/mmc	4.223	4.223	5.114	90	90	120	[27]
δ-$Cu_{33}Al_{17}$	*hR*156	*R*3*m*	12.29	12.29	15.15	90	90	120	[28]
δ-$Cu_{33}Al_{17}$	*hR*52	*R*3*m*	8.707	8.707	8.707	89.74	89.74	89.74	[29]
γ_1-Cu_9Al_4	*cP*52	*P*-43*m*	8.707	8.707	8.707	90	90	90	[30]

Table 4. Planar lattice disregistry between η-Cu_6Sn_5 and γ_1-Cu_9Al_4 or δ-$Cu_{33}Al_{17}$ for measured interfaces using Bramfitt model [36].

Orientation relationship	$(1\bar{2}10)_{Cu6Sn5} \parallel (10\bar{1})_{Cu9Al4}$		$(1\bar{2}10)_{Cu6Sn5} \parallel (10\bar{1})_{Cu33Al17}$		
	$[0001] \parallel [111]$		$[0001] \parallel [111]$		$[0001] \parallel [1\bar{1}1]$
Interfacial planes	$(10\bar{1}0)\&(\bar{1}2\bar{1})$	$(11\bar{2}0)\&(1\bar{1}0)$	$(10\bar{1}0)\&(\bar{1}2\bar{1})$	$(11\bar{2}0)\&(1\bar{1}0)$	$(11\bar{2}0)\&(1\bar{1}0)$
Disregistry	2.22%	2.31%	2.30%	2.49%	2.48%

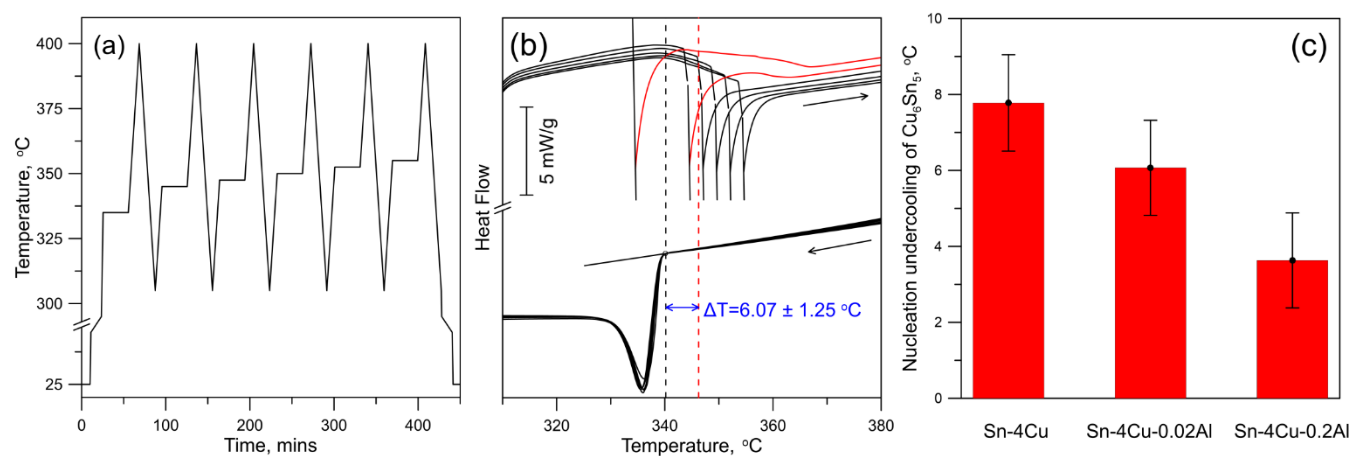

Figure 1. (a) Cyclic DSC programme. (b) Typical DSC experiment and definition used for nucleation undercooling of Cu_6Sn_5 in a Sn-4Cu-0.02Al sample. See Methods section for detail. (c) Mean nucleation undercooling of Cu_6Sn_5 for different Al levels. Error bars show standard deviations from 5 measurements.

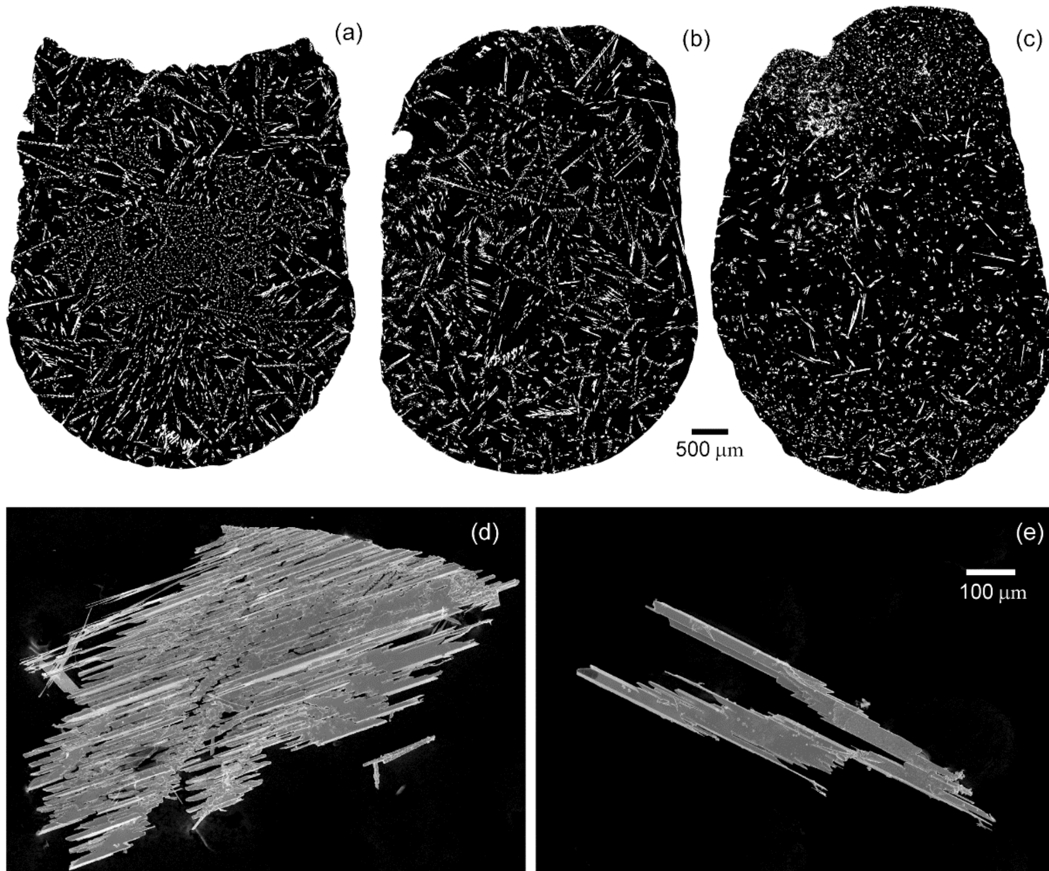

Figure 2. Cu_6Sn_5 microstructure for different Al levels after cooling at ~1K/s. (a)-(c) Optical micrographs of (a) Sn-4Cu, (b) Sn-4Cu-0.02Al, (c) Sn-4Cu-0.2Al. Cu_6Sn_5 is bright. (d)-(e) SEM images of typical (d) partial Cu_6Sn_5 crystal from Sn-4Cu and (e) single Cu_6Sn_5 crystal from Sn-4Cu-0.2Al after selective dissolution of βSn. Note that (a-c) share the same scale bar, so as (d-e).

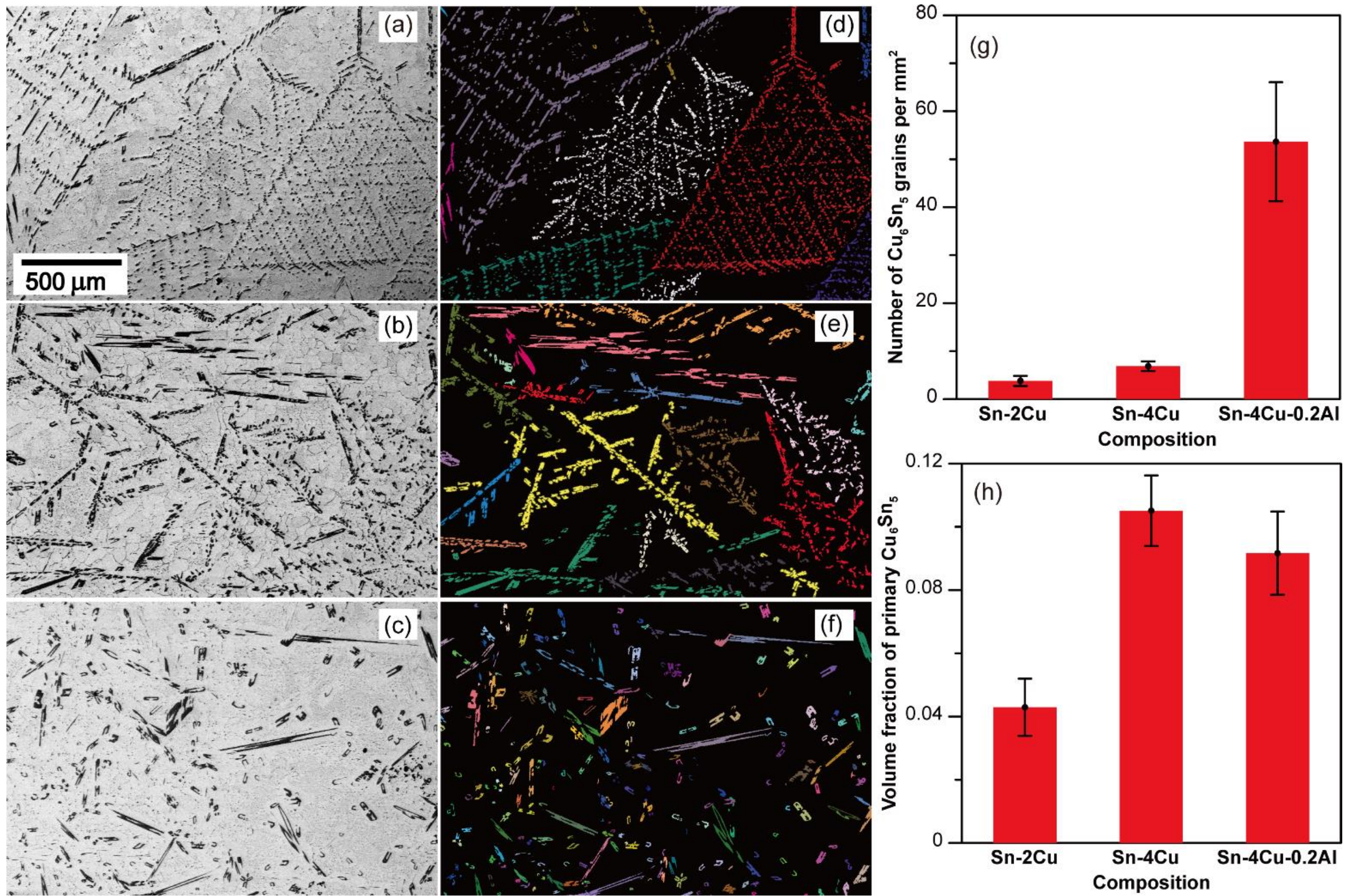

Figure 3. (a-c) BSE-SEM images of typical regions in (a) Sn-2Cu, (b)Sn-4Cu and (c) Sn-4Cu-0.2Al. (d-f) extrapolated EBSD orientation maps showing Cu_6Sn_5 phase of the regions in (a) (b) and (c) respectively. The scale is the same in (a)-(f). (g) Mean and standard deviation of the number density of Cu_6Sn_5 grains based on EBSD maps such as (d) (e) and (f). Error bars come from 4 maps for each composition. (h) Volume fraction of primary Cu_6Sn_5 grains based on optical micrographs.

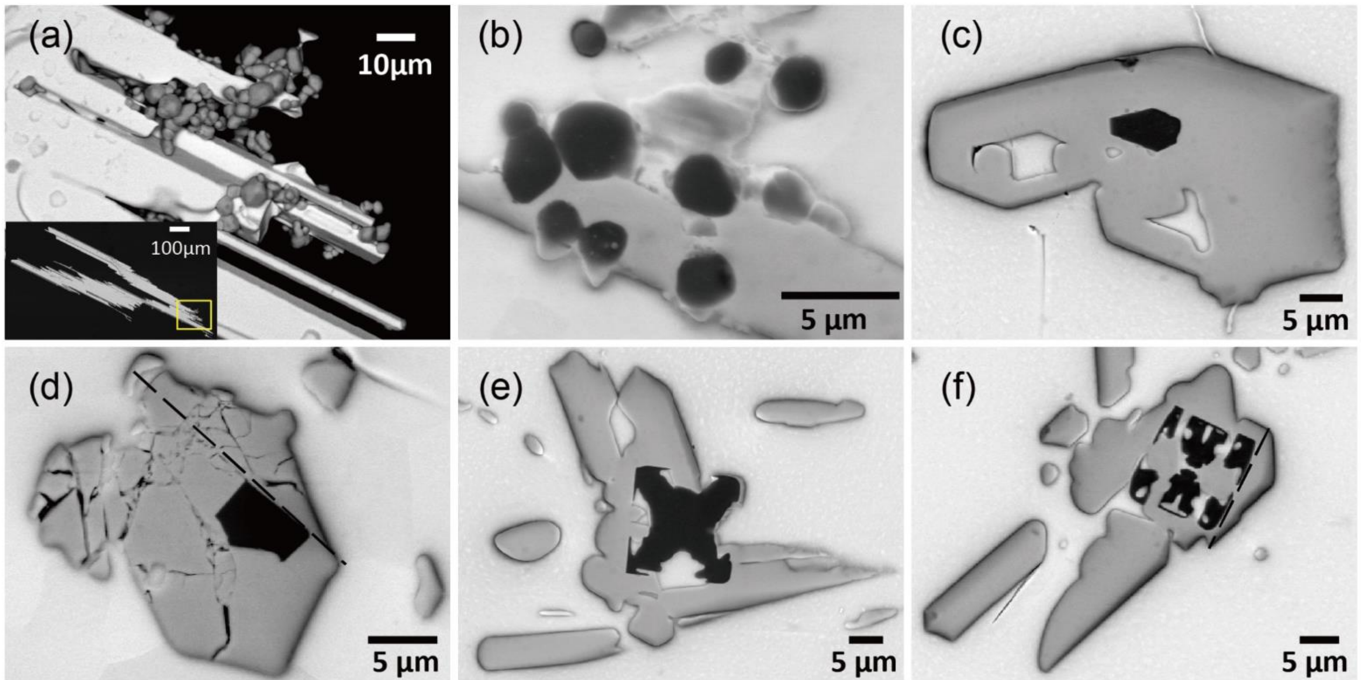

Figure 4. A representative spectrum of Cu_xAl_y particle morphologies observed in Sn-4Cu-0.2Al. (a-f) are BSE-SEM images. Cu_xAl_y is darkest grey, Cu_6Sn_5 is mid-grey and βSn is lightest grey. (a) image after selective dissolution of βSn. A cluster of Cu_xAl_y particles is attached to a Cu_6Sn_5 grain. (b-f) cross sections through Cu_6Sn_5 grains with Cu_xAl_y particles near their centre. Dotted lines highlight the orientation of the Cu_xAl_y-Cu_6Sn_5 interfacial planes relative to the Cu_6Sn_5 growth facets.

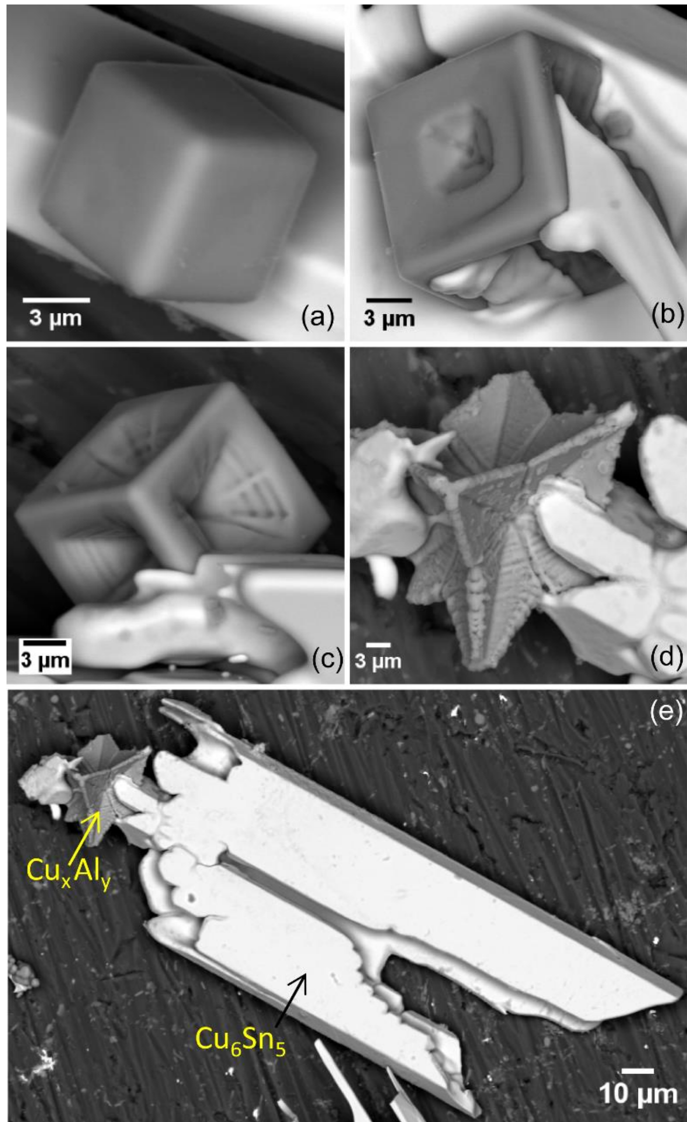

Figure 5. BSE-SEM images of (a-d) typical Cu_xAl_y grains at different stages of growth in Cu-4Cu-0.2Al; (e) typical Cu_6Sn_5 grain growing from the $Cu_{33}Al_{17}$ grain in (d). Note that the magnification decreases from (a) – (e).

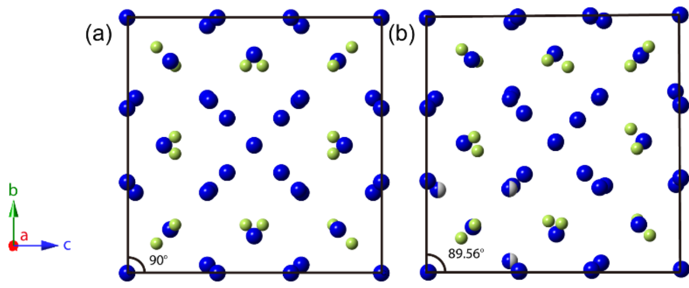

Figure 6. Projection view along [100] in (a) γ_1-Cu_9Al_4 and (b) δ-$Cu_{33}Al_{17}$ based on references [30] and [29] respectively. Dark blue are Cu atoms, green are Al atoms and half-filled spheres represent partially-occupied sites.

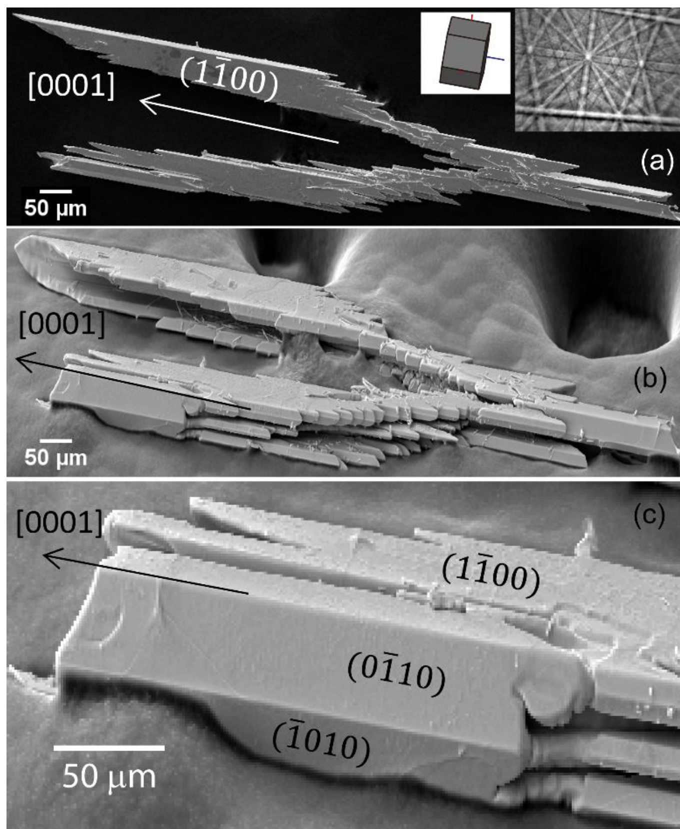

Figure 7. (a) SE-SEM image of a typical Cu_6Sn_5 crystal after selective dissolution of βSn. Insert shows the EBSD pattern from this crystal and the unit cell is used to identify the top facet as ($\mathbf{1\bar{1}00}$) and the [0001] direction; (b) The same Cu_6Sn_5 crystal tilted by 70 degrees in the SEM chamber; (c) Magnified view of (b) showing the side facets are {$\mathbf{1\bar{1}00}$} planes.

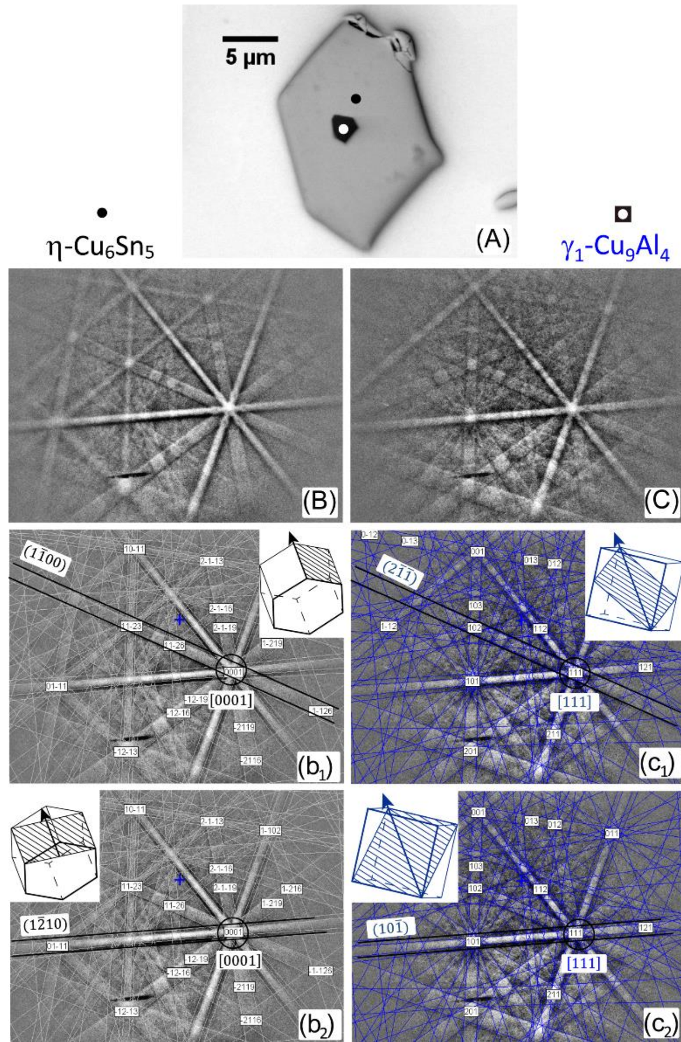

Figure 8. (A) BSE-SEM image of Cu_xAl_y particle within a Cu_6Sn_5 grain; (B) EBSD pattern from Cu_6Sn_5 (black dot in A); (C) EBSD pattern from the Cu_xAl_y particle (white dot in A); (b_1-c_2) EBSD patterns indexed as (b_1-b_2) η-Cu_6Sn_5 and (c_1- c_2) γ_1-Cu_9Al_4. Comparing (b_1) and (c_1) highlights common plane $(\mathbf{1\bar{1}00})||(\mathbf{2\bar{1}\bar{1}})$ and common direction $[\mathbf{0001}]||[\mathbf{111}]$. Comparing ($b_2$) and ($c_2$) highlights common plane $(\mathbf{1\bar{2}10})||(\mathbf{10\bar{1}})$ with common direction $[\mathbf{0001}]||[\mathbf{111}]$.

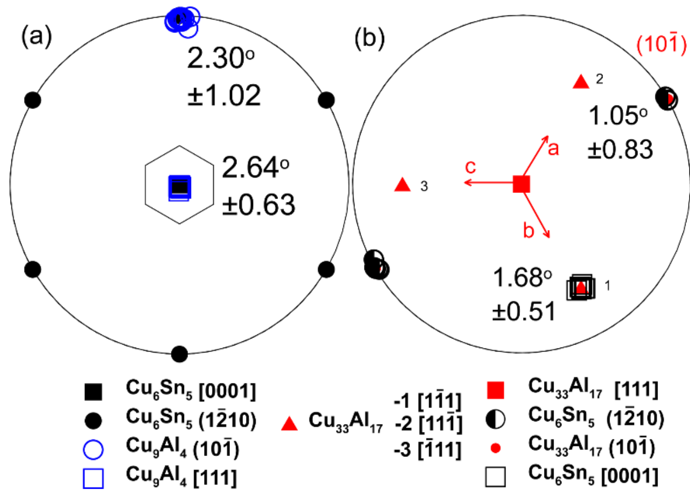

Figure 9. Stereographic projections (a) experimentally determined OR of 17 measured Cu_9Al_4 orientations plotted with respect to Cu_6Sn_5 in direction [0001]. Black hexagon shows the orientation of Cu_6Sn_5. The angular variations of the common direction and planes are labelled with standard deviations. (b) shows 10 (defined as OR_2) of the 17 measured Cu_6Sn_5 orientations plotted with respect to δ-$Cu_{33}Al_{17}$ in direction [111]. Red arrows show the orientation of δ-$Cu_{33}Al_{17}$.

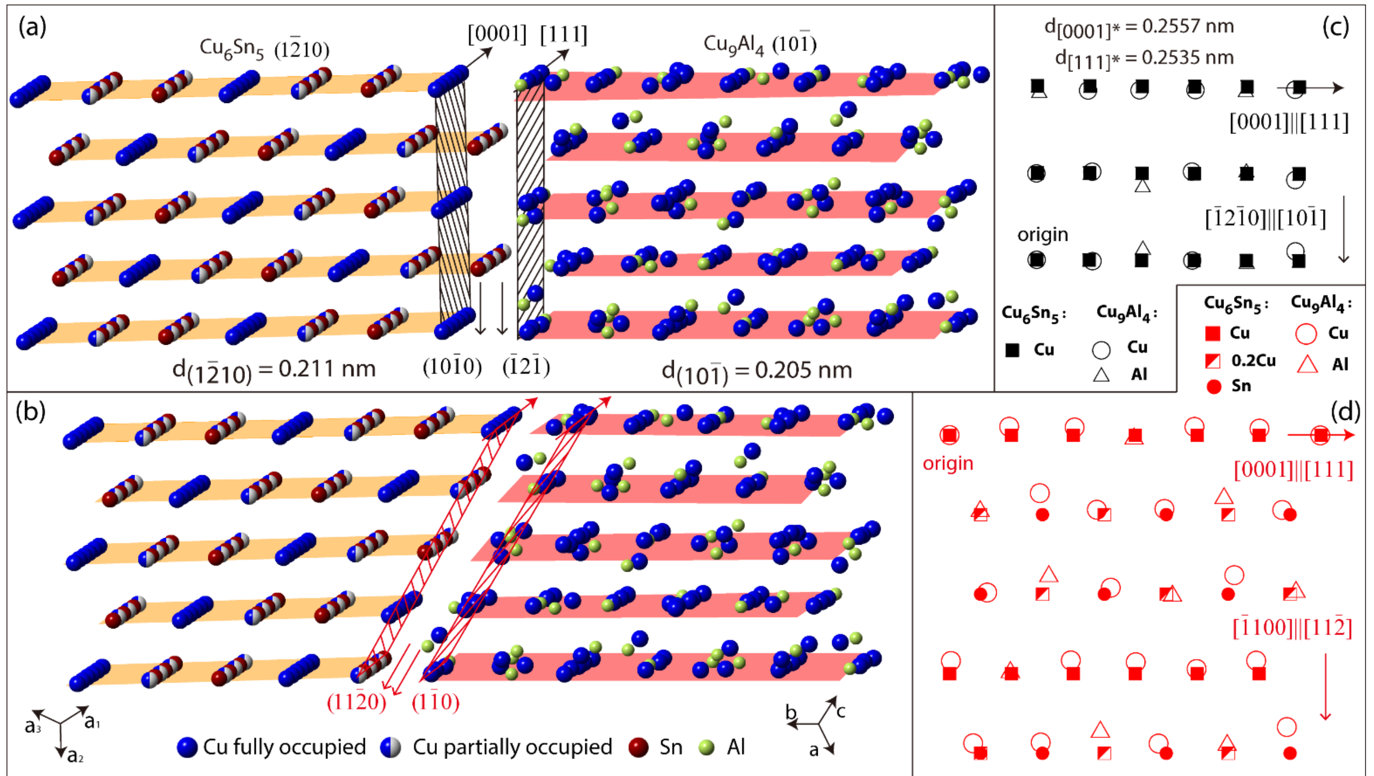

Figure 10. Lattice match in the OR between η-Cu_6Sn_5 and γ_1-Cu_9Al_4 and two interfacial planes. (a-b) 3D representation of OR with parallel close-packed planes (highlighted planes) and close-packed directions in both phases. Black and red shaded planes represent two interfacial planes. (c-d) show planar lattice match of the corresponding interfacial planes in (a-b).

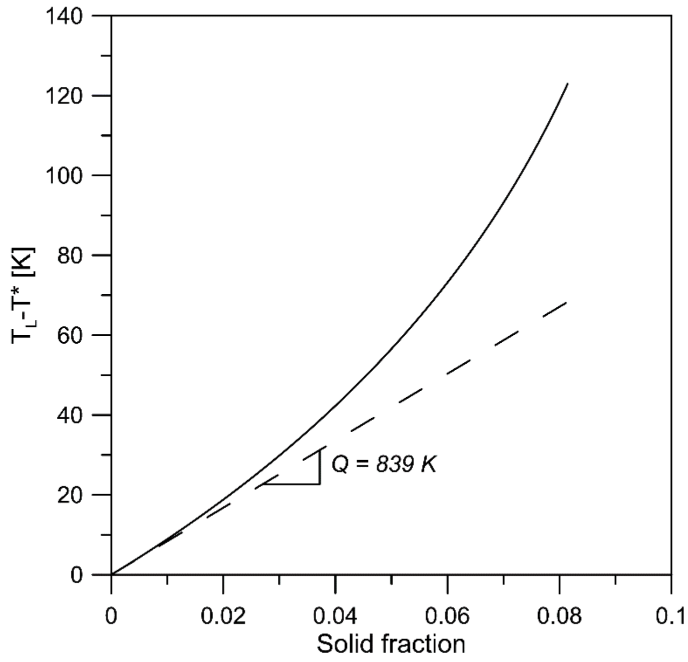

Figure 11. Plot of solutal undercooling (T_L-T*) versus solid fraction for Sn-4wt%Cu using phase diagram data from [20]. The gradient as $\boldsymbol{f_s} \rightarrow \mathbf{0}$ is the growth restriction factor, $\boldsymbol{Q}$= 839K.